Title

Cone-beam CT sampling incompleteness: analytical and empirical studies of emerging systems and source-detector orbits.

Journal

Journal of Medical Imaging, 10(3)

ISSN

2329-4302

Authors

Wu, Pengwei

Tersol, Aina

Clackdoyle, Rolf

et al.

Publication Date

2023-05-01

DOI

10.1117/1.JMI.10.3.033503

Peer reviewed

JMI Journal of Medical Imaging

RESEARCH PAPER

Cone-beam CT sampling incompleteness: analytical and empirical studies of emerging systems and source–detector orbits

Pengwei Wu[a], **Aina Tersol**[a], **Rolf Clackdoyle**[b], **John M. Boone**[c] and **Jeffrey H. Siewerdsen**[a,d,*]

[a]Johns Hopkins University, Department of Biomedical Engineering, Baltimore, Maryland, United States
[b]Université Grenoble Alpes, CNRS, Grenoble INP, TIMC Laboratory, Grenoble, France
[c]University of California – Davis, Department of Radiology, Sacramento, California, United States
[d]The University of Texas M. D. Anderson Cancer Center, Department of Imaging Physics, Houston, Texas, United States

ABSTRACT. **Purpose:** Motivated by emerging cone-beam computed tomography (CBCT) systems and scan orbits, we aim to quantitatively assess the completeness of data for 3D image reconstruction—in turn, related to "cone-beam artifacts." Fundamental principles of cone-beam sampling incompleteness are considered with respect to an analytical figure-of-merit [FOM, denoted $\tan(\psi_{\text{min}})$] and related to an empirical FOM (denoted z_{mod}) for measurement of cone-beam artifact magnitude in a test phantom.

Approach: A previously proposed analytical FOM [$\tan(\psi_{\text{min}})$, defined as the minimum angle between a point in the 3D image reconstruction and the x-ray source over the scan orbit] was analyzed for a variety of CBCT geometries. A physical test phantom was configured with parallel disk pairs (perpendicular to the z-axis) at various locations throughout the field of view, quantifying cone-beam artifact magnitude in terms of z_{mod} (the relative signal modulation between the disks). Two CBCT systems were considered: an interventional C-arm (Cios Spin 3D; Siemens Healthineers, Forcheim Germany) and a musculoskeletal extremity scanner; Onsight3D, Carestream Health, Rochester, United States)]. Simulations and physical experiments were conducted for various source–detector orbits: (a) a conventional 360 deg circular orbit, (b) tilted and untilted semi-circular (196 deg) orbits, (c) multi-source (three x-ray sources distributed along the z axis) semi-circular orbits, and (d) a non-circular (sine-on-sphere, SoS) orbit. The incompleteness of sampling [$\tan(\psi_{\text{min}})$] and magnitude of cone-beam artifacts (z_{mod}) were evaluated for each system and orbit.

Results: The results show visually and quantitatively the effect of system geometry and scan orbit on cone-beam sampling effects, demonstrating the relationship between analytical $\tan(\psi_{\text{min}})$ and empirical z_{mod}. Advanced source–detector orbits (e.g., three-source and SoS orbits) exhibited superior sampling completeness as quantified by both the analytical and the empirical FOMs. The test phantom and z_{mod} metric were sensitive to variations in CBCT system geometry and scan orbit and provided a surrogate measure of underlying sampling completeness.

Conclusion: For a given system geometry and source–detector orbit, cone-beam sampling completeness can be quantified analytically (in terms arising from Tuy's condition) and/or empirically (using a test phantom for quantification of cone-beam artifacts). Such analysis provides theoretical and practical insight on sampling effects and the completeness of data for emerging CBCT systems and scan trajectories.

 [DOI: 10.1117/1.JMI.10.3.033503]

*Address all correspondence to Jeffrey H. Siewerdsen, JHSiewerdsen@mdanderson.org

Keywords: cone-beam computed tomography; image quality; quality assurance; C-arm; non-circular orbits; cone-beam artifacts; completeness; Tuy's condition; source–detector orbits

Paper 22367GR received Dec. 28, 2022; revised May 6, 2023; accepted May 19, 2023; published Jun. 7, 2023.

1 Introduction

Cone-beam computed tomography (CBCT) systems are increasingly being used in dental,[1] breast,[2] otolaryngology,[3,4] orthopedic,[5] and many interventional imaging scenarios.[6–8] Among the challenges to image quality for such systems are artifacts associated with cone-beam sampling incompleteness, commonly observed as "cone-beam artifacts." For a typical orbit consisting of a single circular orbit of a point source and flat detector, cone-beam artifacts are primarily evident as streaks, shading, and/or distortion of edges that are oriented parallel to the axial plane.[9–13] In clinical scenarios, such artifacts can be produced, for example, by vertebral endplates or other bone/joint surfaces parallel to the axial plane and increase in severity at greater distance from the central axial plane.[14]

Motivated by a variety of improvements in 3D imaging performance to be gained from source–detector orbits other than a single circular orbit, many CBCT systems have been proposed or emerged in recent years with alternative orbits.[14–21] In addition to improving cone-beam sampling completeness, such advances could achieve a variety of other potential advantages, including increasing the field-of-view (FOV), reducing metal artifacts,[16,20,21] and improving the spatial-frequency-dependent signal-to-noise ratio (SNR) and task-based imaging performance.[17] CBCT systems capable of such orbits include robotic C-arms [e.g., Zeego and Pheno (Siemens Healthineers)], mobile C-arms with multi-axis motorization [e.g., Cios Spin (Siemens Healthineers) and Vision (Ziehm)], multi-axis motorized radiography [e.g., RAX (Siemens Healthineers)], multi-source breast imaging [IZOview (Izotropic)], and extremity scanning [e.g., OnSight (Carestream)].

Meanwhile, emerging standards for CBCT image quality evaluation recognize the need to quantitatively assess performance beyond conventional scalar (and often subjective) metrics that tend to be limited to the axial plane.[22,23] These include a more rigorous evaluation of fully 3D signal and noise transfer characteristics, including the modulation transfer function (MTF),[24,25] noise-power spectrum (NPS),[23] as well as standard metrics of uniformity and contrast assessed in axial and non-axial planes. By comparison, figures of merit (FOMs) for the completeness of sampling (and the magnitude of associated cone-beam artifacts) have been the subject of individual research reports but have yet to be standardized despite the emergence of clinical systems with more complex source–detector orbits.

A starting point for theoretical considerations of CBCT sampling completeness is Tuy's condition,[26] which addresses the intrinsic tomographic capability of a scanner configuration. The relative positions ("vertices") of the x-ray source–detector trajectory and the object being imaged determine whether a complete 3D reconstruction of the object can be achieved. In this context, a source "trajectory" (alternatively, "orbit") is the path along which the x-ray source travels with projections acquired at some number of vertices along the path. Examples abound with many recognized in early literature on the completeness of cone-beam sampling.[9,27–29] Tuy's condition is geometrical: it requires that every plane that intersects the object must contain an x-ray source location. If Tuy's condition is not satisfied, then a mathematically stable reconstruction of the object function is not possible.[30] On the other hand, if Tuy's condition is satisfied, and in addition, the object remains within the FOV of the scanner, then a mathematically exact (complete) reconstruction is possible from ideal cone-beam projections. We note here that (a) "mathematically stable" refers to the fact that the mathematical operator that models the reconstruction process is continuous (in suitable function spaces) and (b) "mathematically exact" means that an inverse operator exists on which reconstruction can be based.

A "local" version of Tuy's condition exists in which a sub-region [region of interest (ROI)] of the object is considered,[26,30] requiring that each plane that intersects the ROI must contain an x-ray source location. Failure to meet the condition precludes stable reconstruction of the ROI, and satisfaction of the condition permits exact reconstruction if the entire object (not just the ROI) is within the FOV. The above statements regarding completeness of reconstruction assume the absence of prior information on the object. Hence, for the common scenario of a single circular trajectory, a 2D axial ROI in the plane of the source trajectory can be reconstructed, but any off-plane region cannot be exactly recovered from cone-beam projections.

To describe the extent to which Tuy's condition fails in various regions of the image, a FOM for sampling completeness can be envisioned such that the scale value depends only on the source–detector trajectory and not on the object. Description in such terms serves to elevate the rigor of performance analysis beyond ad hoc, hand-crafted metrics of artifact magnitude. Moreover, such an objective metric could quantify the extent to which departures from Tuy's condition, however small, may still support approximate reconstruction. While the correlation of such an FOM with artifact magnitude would still be dependent on the object being imaged (e.g., its shape, orientation, and contrast), an objective FOM for cone-beam sampling completeness could permit intercomparison of various system designs and thereby assist system developers in understanding the gains that may be obtained from alternative system geometries/trajectories.

Over the past 20 years, several such FOMs have been proposed. Some authors[20,31,32] considered the fraction of planes intersecting at each voxel that contains an x-ray source location. If the fraction is 1.0, then Tuy's condition is satisfied at that voxel, and fractions <1.0 correspond to an increased potential for cone-beam artifact at that location. Other authors[33,34] computed a FOM that can accommodate a finite number of source locations or as a continuous trajectory: for each plane passing through the voxel, the sine of the angle of the nearest source location is calculated, and an angle of zero means that the plane contains an x-ray source location; averaging these values over all planes[33] (or alternatively, taking the maximum value[34]) provides a FOM that correlates with sampling completeness at that location. Alternatively, the information for each plane need not be combined, and the angular values corresponding to all planes intersecting the voxel are considered in full.[11,35] An entirely different approach, based not on Tuy's condition but on a local parallel-beam geometry, uses a local Fourier representation and identifies a cone of unmeasured 3D Fourier components at each voxel.[10] For voxels at which the cone degenerates to a line, Tuy's condition is satisfied. In each of these cases, the FOM provides a map of local "Tuy values" but cannot be interpreted directly in terms of data completeness for exact reconstruction, because the condition of the object lying inside the FOV was not considered. A more detailed review of such sampling incompleteness FOMs can be found in Ref. 11.

In this work, we consider a theoretical FOM that depends on the normal directions of the intersecting planes at each voxel.[11] For each such plane, we identify $\psi_{\min}$ as the angle of the closest source point. A useful interpretation of this value is that the tangent ($\tan \psi_{\min}$) is the smallest gap between two small, parallel unit disks that can be visibly separated in an ideal reconstructed image. Taking $\tan \psi_{\min}$ as an analytical FOM in this work, we evaluate this FOM in a variety of CBCT system geometries.

Compared with other metrics mentioned above, $\tan \psi_{\min}$ has a number of helpful advantages. It is (a) object-independent (i.e., only depends on system geometry), (b) compatible with non-circular orbits, (c) compatible with discrete source trajectories (as opposed to theoretical continuous source trajectory), (d) fast to calculate, and (e) able to provide positional or spatially dependent completeness assessment across the FOV. Other FOMs in literature typically do not share all these advantages. In addition, $\tan \psi_{\min}$ features a strong link with the concept of resolving the gap between two parallel disks, making it an excellent choice in this work considering that our test objects are also composed of parallel disks as descried below.

A test phantom referred to as the Corgi™ (The Phantom Lab, Greenwich, New York, United States) has been developed for routine assessment of CBCT image quality and fully 3D signal and noise transfer characteristics, and it includes a series of disk-pair inserts designed to quantitatively characterize the magnitude of cone-beam artifacts. Disk pairs present a commonly employed feature for which sampling incompleteness is fairly well described: specifically, the spatial frequency content of the disk pairs is largely along the longitudinal (f_z) axis—i.e., within

the unsampled "null cone" of frequency space for a simple circular orbit. In the work detailed below, a series of experiments were performed to investigate the relationship between analytical considerations based on Tuy's condition (i.e., tan $\psi_{\min}$) and image quality as empirically quantified in the test phantom (i.e., modulation of voxel values between the disk pairs, denoted z_{mod} below). A simulation study was also conducted to (a) probe the relationship between tan $\psi_{\min}$ and an alternative FOM for cone-beam sampling completeness (viz., the volume of the Fourier domain null cone) and (b) evaluate correlation of tan $\psi_{\min}$ with z_{mod} as a surrogate for the underlying completeness of sampling. Phantom experiments were conducted with two CBCT systems (a single-source mobile C-arm and a multi-source O-arm) and a range of source–detector orbits, including (a) a standard circular orbit, (b) tilted circular orbits, (c) a three-source circular orbit, and (d) a non-circular orbit [sine-on-sphere (SoS)]. In each case, we analyze the analytical and empirical FOMs related to the completeness of cone-beam sampling. Initial studies were presented in SPIE Proceedings,[36] and the work presented below represents a substantial expansion of that work, including: (a) expanded discussion of theoretical foundation for analytical FOM for cone-beam sampling completeness, (b) simulation studies that relate such theoretical foundations to features as they might present in an empirical test phantom (e.g., a sphere or disk pair), and (c) additional experiments, including a CBCT system featuring a multi-source system geometry.

2 Methods

2.1 Analytical Basis for Cone-Beam Sampling Incompleteness

The principle behind Tuy's condition is the inversion formula for the 3D Radon transform. A plane integral is the sum of the density of the object that lies within a certain plane. From all plane integrals of the object, the 3D Radon inversion formula can be used to reconstruct the object density function.[37] If a cone-beam projection is not truncated (which is ensured if the object lies within the FOV), then plane integrals can be approximated for all planes that contain an x-ray source. The approximation becomes exact when derivatives are considered, and the 3D inversion formula can work with derivatives instead of raw plane integrals. Therefore, if Tuy's condition is satisfied, then all (differentiated) plane integrals can be obtained from the cone-beam projections, and exact reconstruction via the 3D inversion formula is possible. A similar argument works for the local version of Tuy's condition with respect to a ROI.

Conversely, if a plane passes through some part of the object containing no x-ray source location, Finch pointed out that an object with discontinuous density along that plane could still have completely smooth projection data for every projection.[30] Consequently, in a specific yet broad mathematical sense, this object function cannot be stably reconstructed, irrespective of the algorithm applied (unless strong a priori information is included).[30] This idea of a discontinuous object provides motivation for the "two-parallel disks" phantom used to illustrate the difficulty when there is no x-ray source on a plane passing between the disks.

The analytic FOM examined in this work depends not only on the location in the object but also on a direction. The notation $I(Q, \mathbf{n})$ refers to the "incompleteness" FOM at location Q and in the direction $\mathbf{n}$ (where $\mathbf{n}$ is a 3D unit vector), as depicted in Fig. 1(a). This FOM is purely geometric and depends only on the positions of the x-ray source(s). In practice, there are only a finite number of source locations, and we use i for the view index. Given a specific location Q, and a direction $\mathbf{n}$, we consider the plane passing through Q and perpendicular to $\mathbf{n}$. If an x-ray source, S_i, happens to actually lie exactly on this plane, then $I(Q, \mathbf{n}) = 0$. If not, then we examine every x-ray source and determine, which is the closest to being on the plane in an angular sense. For every source location S_i, we compute the quantity ψ_i, which is the angle defined by the line from S_i to Q with the plane (which contains Q). Therefore, $0 <= \psi_i <= \frac{\pi}{2}$, and we define the FOM for incompleteness as

$$I(Q, \mathbf{n}) = \min\{\tan \psi_i : \ i = 1,2, \ldots, \mathbf{n}\}. \tag{1}$$

The situation of the x-ray source traversing an arbitrarily tilted circular orbit is illustrated in Fig. 1(a). The source travels in the x-y plane, where $y = y'$, and the x-y plane has been rotated by the tilt angle α. For view-index i, the vector $\overline{\mathbf{v}}_i$ points to the source location from the point Q. The angle between this vector and the plane perpendicular to $\mathbf{n}$ is denoted ψ_i. Throughout this paper, we take $\mathbf{n}$ always to be parallel to the z-axis.

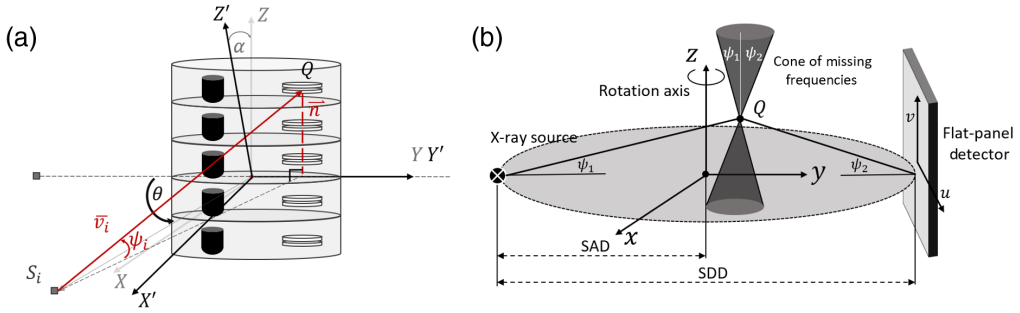

Fig. 1 System geometry and cone-beam sampling incompleteness. (a) Illustration of cone-beam geometry and the ray angle, ψ, for a given position in the field of view. The geometry is depicted with respect to evaluation of cone-beam sampling incompleteness analytically [in terms of $\tan \psi_{\text{min}}$] and in the context of a test phantom (Fig. 2) containing disk pairs in which sampling incompleteness can be measured experimentally [in terms of signal modulation (z_{mod}) between disk pairs]. For a tilted circular orbit, the tilt angle is denoted α (e.g., the tilt of a C-arm gantry). (b) Fourier domain depiction of sampled frequencies (and the "null cone") for a single-source, circular orbit.

An alternative metric of incompleteness was described by Bartolac et al.[10] in terms of the extent of the local Fourier "null cone." The concept is based on the Fourier slice theorem applied to 3D parallel projections. If a very small neighborhood is considered about the image location Q, the rays coming from each cone-beam source will appear parallel when they arrive in the neighborhood, and a plane of local 3D measured frequencies can be identified that pass through the point Q and are perpendicular to the line from Q to the source. Each x-ray source contributes a Fourier plane in this manner, and the "null cone" refers to a region of 3D Fourier space, which is empty of planes, as shown in Fig. 1(b) for the case of a circular x-ray orbit.

We propose a FOM based on the null cone, specifically, the normalized volume of the intersection of the null cone with a unit sphere (solid sphere) centered at Q, the vertex of the cone. The larger the volume, the more incomplete the data at location Q. It is straightforward to see that the volume is zero (the cone degenerates to a line) if and only if Tuy's condition is satisfied at Q. (In the usual situation of a finite number of projections measured along a circular orbit, the null cone will have polygonal sides. We refer to this Fourier region as the "null cone" even for a finite number of views and for non-circular orbits, where its shape may depart from that of a cone.) A variety of disadvantages of this FOM are worth noting. First, it describes a continuous approximation of the Fourier domain associated with trajectories that are a union of smooth curves, not a finite sampling along the trajectory, which occurs in practice. Furthermore, it does not easily translate to the general scenario of non-circular trajectories, presenting a cumbersome calculation for general non-circular orbits (including short-scan trajectories). However, a direct measurement of the null cone could be achieved by imaging a small stimulus, such as a small dense sphere, and computing the local 3D Fourier transform of the reconstructed image. Note also that the particular image reconstruction method can affect such a measurement. Finally, the method is difficult to interpret for short scan or a super-short-scan trajectories for which the missing Fourier region may not simply be a closed cone.

For a circular orbit, the null cone FOM can be related to the proposed analytical FOM, $\tan \psi_{\text{min}}$. Taking $\mathbf{n}$ to be perpendicular to the plane of the circle, and assuming a null cone with a constant aperture ψ [i.e., $\psi_1 = \psi_2$ in Fig. 1(b)— i.e., a point on the z axis—the normalized null cone volume is $1 - \cos \psi$, and $I(Q, \mathbf{n}) = \tan \psi$. Both FOMs are monotonic in ψ with a minimum value of zero. For other locations, the null cone has variable aperture, and the volume can be reasonably approximated by $1 - \cos \psi_{\text{avg}}$ where ψ_{avg} is the average value of ψ taken over each x-ray source location. On the other hand, $I(Q, \mathbf{n}) = \tan \psi_{\text{min}}$ corresponds to a cone with the minimum aperture and thus appears to underestimate the incompleteness specified by the null cone. For a tilted circular trajectory, on the other hand, the volume of the tilted null cone would overestimate the incompleteness of sampling, as it attempts to describe a single incompleteness measure at each location, irrespective of the orientation of the scanning geometry. This apparent

discrepancy between the two FOMs simply reflects the fact that at each location (Q), the null cone volume gives an overall incompleteness metric, whereas tan $\psi_{\min}$ stratifies incompleteness according to the direction of rays $\mathbf{n}$ through that location.

2.2 Test Phantom for CBCT Image Quality Evaluation

The Corgi™ Phantom (The Phantom Lab, Salem, New York, United States) is based on principles described in Ref. 23 presents a set of cylindrical slab modules (135 mm diameter, 40 mm thick) that can be configured in various arrangements along its length. Two module types are available: a homogeneous module for assessment of uniformity and NPS, and a test module containing inserts for measurement of Hounsfield unit linearity, contrast, and MTF (in three dimensions), along with Teflon disk pairs that can be used to quantify the magnitude of cone-beam artifact. Through-holes spanning the length of the phantom allow insertion of pencil or thimble ion chambers for measurement of air kerma. The nominal phantom configuration [three homogeneous modules and two test] was extended in this work to a long configuration of nine modules spanning 360 mm as shown in Fig. 2, with five test modules in the middle and two homogeneous modules at each end. Such a long configuration was well suited to this study because it presented Teflon disk-pair test objects at various z positions throughout the longitudinal FOV; meanwhile, the homogeneous modules at the ends extended the phantom beyond the FOV in the z direction such that the flat surfaces at extrema did not contribute to measurements of cone-beam artifact.

This study focused on the disk pairs for measurement of cone-beam artifacts. Each test module contains a pair of 1.0 mm thick Teflon disks (each 25 mm diameter) separated by 1.0 mm of uniform polyurethane (same bulk material as the rest of the module). Because the distance between the disk pairs is 1.0 mm, meaningful measurements require 3D image reconstructions with slice thickness <1 mm (e.g., 0.3 to 0.4 mm in the studies described below). The center of the Teflon disk pair is offset from the center of the phantom by 40 mm as illustrated in Figs. 1 and 2. The magnitude of cone-beam artifact was defined in terms of the modulation of the z-direction signal profile extracted through the disks as illustrated in Figs. 2(c)–2(d). The modulation is termed z_{mod}, defined as

$$z_{\text{mod}} = \left| \frac{\mu_{\max} - \mu_{\min}}{\mu_{\max} - \mu_0} \right|, \tag{2}$$

where $\mu_{\max}$ is the peak voxel value in the disks (averaged between the two disks for each longitudinal profile through the disks), $\mu_{\min}$ is the minimum voxel value in the region between the disks (similarly averaged for each longitudinal profile), and μ_0 is mean background voxel value in the external regions outside (above and below) the disks. The z_{mod} metric is relative,

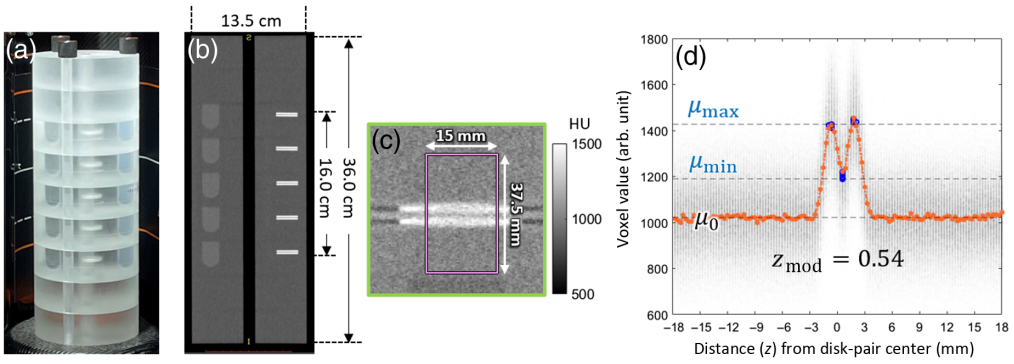

Fig. 2 Test phantom and disk-pair inserts (oriented orthogonal to the long axis of the phantom) for analysis of cone-beam artifacts. (a) Photograph of the long stack of five test modules used in this study. (b) Sagittal slice of the phantom acquired on a diagnostic helical CT scanner. (c) ROI for one example disk pair imaged on a CBCT system. (d) Longitudinal signal profiles through the disk pair in (c), illustrating reduced signal modulation between the disks ($z_{\text{mod}} < 1$) for incomplete cone-beam sampling.

scales independently of the Hounsfield scale, and is bounded on the interval 0 to 1. A value of $z_{\text{mod}} = 1.0$ therefore represents full modulation and absence of cone-beam artifact, whereas lower values correspond to a loss of modulation and more severe cone-beam artifacts. Regions outside the "medial" and "lateral" to the disks [e.g., dark streaks evident in Fig. 2(c)] were not evaluated in this work, as they include cone-beam and other effects (e.g., beam hardening). In this way, z_{mod} presents an empirical FOM for cone-beam artifact magnitude for comparison to the analytical FOM, $\tan \psi_{\text{min}}$.

2.3 Simulation Studies: System Geometry and 3D Image Reconstruction

The various FOMs for cone-beam sampling incompleteness were evaluated in a series of studies beginning with digital simulation (denoted Simulation #1 and #2, below) and extended to a series of four physical experiments performed with the test phantom and increasingly complex source–detector orbits: i.e., (Experiment #1) a single-source, untilted circular orbit; (Experiment #2) a single-source, tilted circular orbit; (Experiment #3) multiple-source, circular orbit and (Experiment #4) a single-source, non-circular orbit. Each experiment is further detailed in Sec. 2.4.

All images (simulation and experiments) were reconstructed on a volumetric grid with isotropic voxel size of 0.313 mm × 0.313 mm × 0.313 mm, lateral FOV covering 160 mm × 160 mm (no lateral truncation of the phantom), and longitudinal FOV of 160 mm for simulation studies and the Cios Spin C-arm 200 mm for the extremity scanner (each described below). All images were reconstructed with the penalized least-square (PLS) method with a quadratic loss function to penalize pairwise differences between voxels in the first-order neighborhood around each voxel.[38] The objective function for PLS was minimized using separable quadratic surrogates (SQS) with ordered subsets SQS[39] with 80 iterations and 10 subsets. The PLS method was implemented in MATLAB (The MathWorks, Natick, Massachusetts, United States), with forward projection (using a Siddon forward projector[40]) and back projection (using Peters' back projector[41]) executed on GPU using CUDA-based libraries. All image reconstructions were performed on a workstation equipped with a GeForce GTX TITAN X (NVIDIA, Santa Clara, California, United States) graphics card.

First, two simulation studies were conducted to bridge the concepts between the analytical FOM ($\tan \psi_{\text{min}}$), an idealized probe for cone-beam sampling incompleteness (i.e., a sphere), and the empirical probe (disk pairs and z_{mod}). This objective of this study was to demonstrate that the sampling incompleteness effects are evident in both the sphere and the disk pair, and that the disk pair (and corresponding z_{mod} metric) is a reasonable probe for underlying effects described by $\tan \psi_{\text{min}}$ and the Fourier null cone. Compared to a sphere, a disk pair is much easier to manufacture and to embed in a quality assurance (QA) phantom. While it only probes completeness in one direction (parallel to the z axis), this direction is a natural orientation for many computed tomography (CT) applications. Both simulation studies used a system geometry corresponding to that of the mobile C-arm system (Sec. 2.4.1); however, a full 360 deg scan orbit with 720 projections was used to simplify calculation of the null cone volume.

Simulation #1 involved a 20 mm diameter sphere at seven equally spaced z distances from isocenter (ranging 0 to 60 mm) to illustrate cone-beam artifacts with respect to a simple spherical probe. The null cone volume and $\tan \psi_{\text{min}}$ were calculated as in Sec. 2.1. The magnitude of cone-beam artifacts was also quantified in terms of root-mean-square error (RMSE) between the reconstructed volume and the known truth (simulation object). We hypothesized that sampling incompleteness effects evident in a sphere and analytical FOMs would show clear, negative correlation with RMSE, indicating that a metric, such as $\tan \psi_{\text{min}}$, gives a practical analytical surrogate for sampling incompleteness.

Simulation #2 involved a disk pair with the same specification as in the Corgi phantom at the same seven positions as in Simulation #1. Besides RMSE, the magnitude of cone-beam artifacts was quantified in terms of z_{mod} [Eq. (2)], which unlike RMSE, does not require a truth volume. We hypothesized that cone-beam sampling incompleteness effects would be quantifiably evident in both the sphere and the disk pair objects and that z_{mod} would present a similar trend as RMSE for either the sphere or the disk pair objects, thus indicating that the disk pair (and z_{mod} metric) gives a practical empirical surrogate for sampling incompleteness.

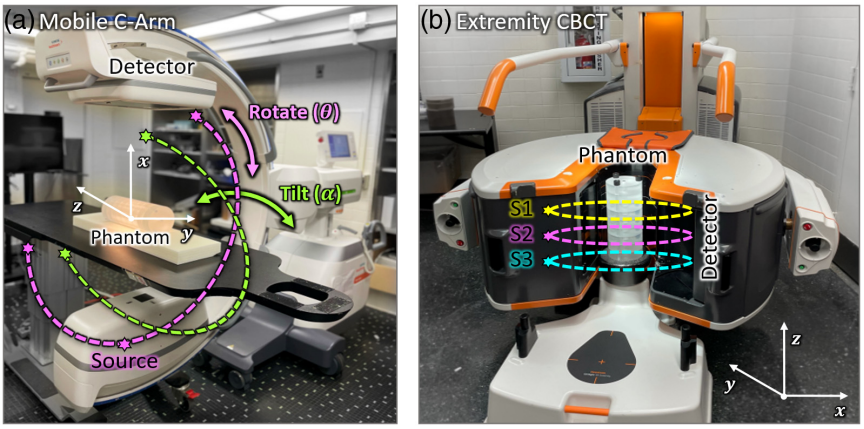

Fig. 3 CBCT systems used for experimental studies. (a) Mobile C-arm capable of circular, tilted, and non-circular SoS scan orbits. (b) Diagnostic extremity scanner including three x-ray sources (S1, S2, S3) capable of (circular) single-source and multi-source scan orbits.

2.4 Physical Experiments: Systems and Source–Detector Orbits

Two CBCT systems with distinct options in source–detector orbits were utilized for physical experiments in this work. The first system was a mobile C-arm (Cios Spin 3D, Siemens Healthineers, Forcheim, Germany), shown in Fig. 3(a). The C-arm allows rotation angle (θ) to vary from 0 deg to 196 deg and tilt angle (α) to vary from -15 deg to 15 deg without table collision. Within a research (non-clinical) setting, the C-arm was also capable of executing non-circular orbits via motorized variation of θ and α during the scan. The system features an x-ray tube with a rotating tungsten anode [0.3/0.5 focal spot (FS)] and an indirect-detection CMOS-based flat panel detector (Xineos 3030 HS, Teledyne Dalsa, Waterloo, Canada) with 300 mm $\times$ 300 mm detector area (0.3 mm $\times$ 0.3 mm pixel size with 2×2 hardware binning). The source-axis distance was 623 mm, and the source–detector distance was 1164 mm, giving a 160 mm $\times$ 160 mm $\times$ 160 mm FOV. A body scan protocol was used, giving 400 projections acquired over a 196 deg scan arc at 110 kV with a 30 s scan time.[42]

The second system was the OnSight 3D Extremity CT System (Carestream Health, Rochester, New York, United States), shown in Fig. 3(b).[14] An interesting aspect of this system is the three-source configuration (denoted "S1," "S2," "S3") consisting of three separate anode-cathode units, separated by 85 mm in the longitudinal/z direction. The cathode-anode axis for each source is oriented perpendicular to the z axis and separately angulated to present nominal 0.6 FS focal spot size at the detector center. The "firing sequence" of the three x-ray sources is controllable via software. In this work, the scan protocol involved 600 projections (with firing sequence S1-S2-S3-S1,..., 200 projections each) acquired over a 210 deg scan arc at 90 kV with a 24 s scan time.

The various orbits investigated in the current work are summarized in Fig. 4.

2.4.1 *Experiment #1: Single-source circular orbit*

Experiment #1 focused on the most typical clinical use case—a single-source, untilted, circular scan, as marked by the dashed green curve in Fig. 3(a). This simple orbit is also illustrated with respect to disk pairs in the test phantom in Fig. 4(a). The analytical and empirical FOMs were evaluated using the test phantom [Fig. 2(a)] and mobile C-arm [Fig. 3(a)].

2.4.2 *Experiment #2: Single-source circular orbit with tilt*

Experiment #2 focused on the effect of a tilted orbit on cone-beam artifact as marked by the green curve in Fig. 3(a). The tilt angle (α) ranged from -15 deg to 15 deg at a 5 deg interval, which is the maximum range permitted by the C-arm system in a clinical setting. The tilted orbit is also illustrated with respect to the disk pairs in the test phantom in Fig. 4(b). A reproducible orbit and geometric calibration (i.e., source–detector pose relationship for all θ) is prerequisite to accurate

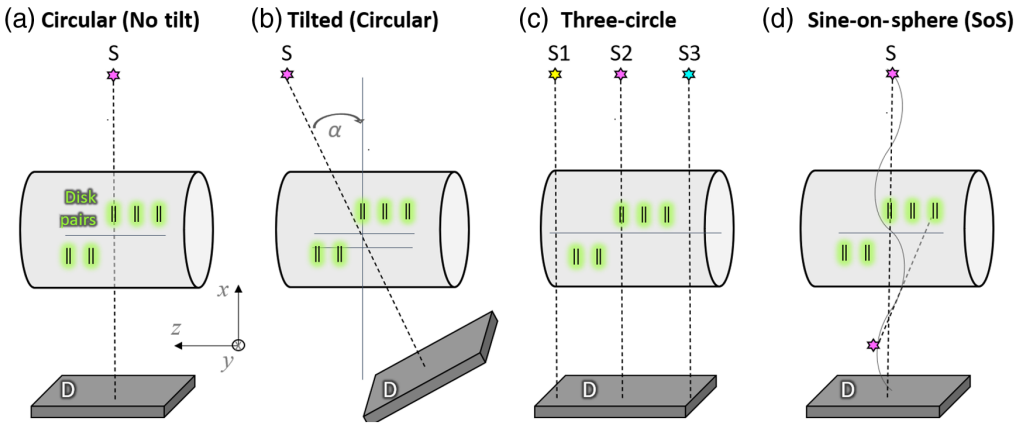

Fig. 4 Illustration of scan orbits, from left to right: "circular orbit" (viz., single circle, short-scan, untilted orbit; "tilted orbit" (viz., single circle, short-scan, tilted orbit); "three-circle orbit" (viz., triple circle, short-scan, untilted orbit) and "SoS orbit" (viz., short-scan, sinusoid on a sphere).

3D image reconstruction and sampling incompleteness FOM calculations. Because the mechanical flex of the gantry depends on α, a separate geometric calibration was obtained for each of the seven tilt angles using the method of Cho et al.[43] with a cylindrical BB phantom oriented at the same tilt angle as the C-arm gantry. For 3D images to be reconstructed in a common coordinate system (i.e., without registration and interpolation, so the same ROI could be used for z_{mod} calculation for all tilt angles), the world coordinate systems for the seven calibrations were rigidly aligned using the method described in Ref. 16.

2.4.3 *Experiment #3: Three-source circular orbits*

Experiment #3 considered the effect of a multi-source (circular) orbit on cone-beam sampling incompleteness. The three-source extremity system in Fig. 3(b) was used, with details of geometric calibration in Ref. 14. The three-source orbit is illustrated with respect to disk pairs in the test phantom in Fig. 4(c). In addition to the system's standard three-source scan protocol with nominal S1-S2-S3-S1 firing sequence, an additional set of three scans were acquired—each with only one source (S1, S2, or S3) energized for each scan. Sampling completeness was evaluated in terms of analytical and empirical FOMs for the three-source configuration in comparison to that for each single-source scan.

2.4.4 *Experiment #4: Single-source SoS orbits*

Finally, Experiment #4 evaluated sampling incompleteness for a non-circular orbit using the mobile C-arm system. In this work, a SoS orbit was configured in which angular increment (θ) increased linearly with view number ($\Delta\theta = 0.49$ deg), whereas α followed a sinusoidal with magnitude $= \pm 15$ deg). The SoS orbit is also illustrated with respect to disk pairs in the test phantom in Fig. 4(d), although a period of 1 was used over the 196 deg scan (400 projections) [more periods are shown in Fig. 4(d) for purposes of illustration]. With respect to Tuy's condition as described in Sec. 2.1, the SoS orbit involves the source following a sinusoidal path on a spherical surface. The principles described by Tuy's condition suggest that the SoS orbit provides complete sampling for every voxel within the 160 mm × 160 mm × 160 mm FOV.[44–46]

3 Results

3.1 Simulation Studies

Figure 5 summarizes results of the simulation studies demonstrating the sampling/completeness effects as evident in a sphere and/or a disk pair. Figure 5(a) shows that the analytical metrics—tan ψ_{min} and null cone volume—increase with distance from isocenter (i.e., from the central axial plane), the former in a linear manner over the range considered. As seen in Fig. 5(b), the

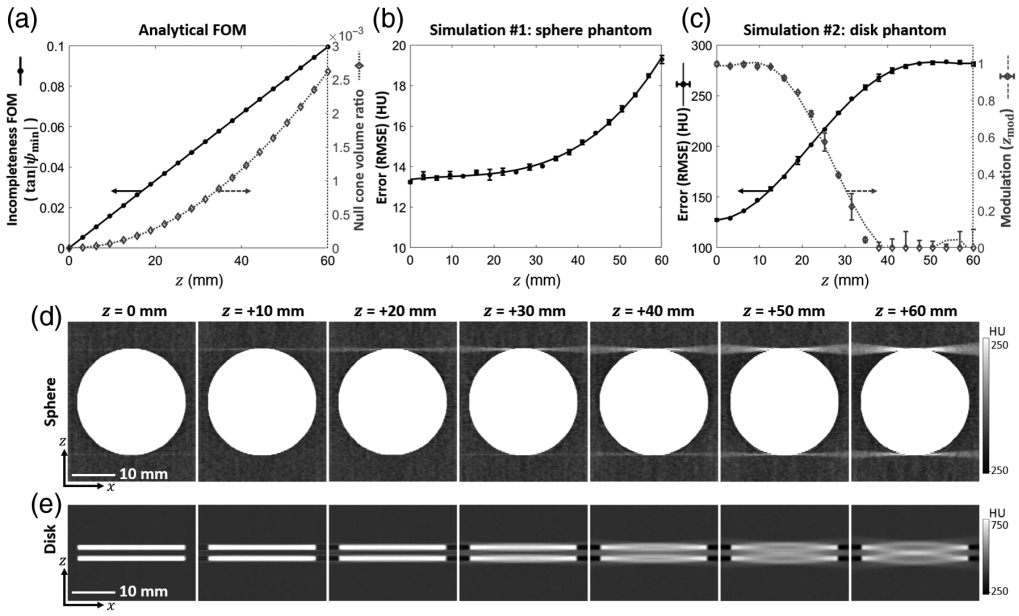

Fig. 5 Simulation studies: evaluation of sampling incompleteness in spheres and disk pairs at various z location. (a) Analytical FOM for incompleteness (left: tan $\psi_{\min}$, right: volume ratio of the null cone) calculated as a function of the (z-direction) distance from the source plane. (b) Empirical FOM for incompleteness (RMSE) measured in a sphere phantom. (c) Empirical FOM for incompleteness (left: RMSE, right: z_{mod}) measured in a disk pair. (d) Coronal views of the sphere phantom at various z locations. (e) Coronal views of the disk phantom at various z locations.

error (RMSE) in image reconstruction (of a sphere) increase with distance from isocenter in a more strongly nonlinear manner for which errors are relatively small over the range 0 to 30 mm from isocenter, beyond which they become sharply more significant. The offset near isocenter (RMSE $\sim$ 13 HU) is attributable to quantum and electronic noise as well as possible cone-beam effects, since the top and bottom edges of the sphere are not exactly at $z = 0$. Figure 5(c) shows that the RMSE for the disk phantom also increases with z and is a sensitive probe of error, increasing by more than 100 HU over the range of FOV investigated. Also shown is the correlation with the empirical metric z_{mod}, which varies over its full range (0 to 1) over the range of FOV investigated. The disk pair therefore presents a sensitive probe and simple quantitation (via z_{mod}) of sampling incompleteness that is consistent with the results of a more idealized test object (a sphere) and, more importantly, with more fundamental analytical metrics, such as tan $\psi_{\min}$ and the null cone volume. Figures 5(d)–5(e) illustrate the effects visually in a coronal image of a sphere and disk pair, where cone-beam artifact is visible at the superior and inferior aspect of the sphere and in a loss of signal modulation in the region between the disks.

3.2 Phantom Studies

3.2.1 *Effect of CBCT orbit*

Figure 6 summarizes the magnitude of cone-beam artifacts measured in terms of the disk pair FOM, z_{mod}. For the untitled circular orbit (i.e., $\alpha = 0$ deg), z_{mod} spans a broad range throughout the FOV, from $\sim$1.0 at the central axial plane to <0.1 at extrema in $\pm z$. This broad range and poor overall performance (i.e., strong cone-beam artifacts at distances far from the central axial plane) reflect the classic shortfall for CBCT imaging with a single source and circular orbit—a broad range in sampling completeness over the volume.

For tilted circular orbits (gantry tilt alpha = 5 deg, 10 deg, 15 deg in Fig. 6), a reduction in artifact magnitude is evident for higher tilt angles (recalling that all disk pairs were oriented orthogonal to the longitudinal axis). The interquartile range (IQR) in z_{mod} reduces markedly and monotonically, with a tilt of 15 deg giving $z_{\text{mod}} > 0.85$ for most disks throughout the volume. It is important to note, of course, that the tilted orbit does not in itself reduce cone-beam effects; rather, it simply reduces the artifacts that are evident in disks in this particular orientation relative

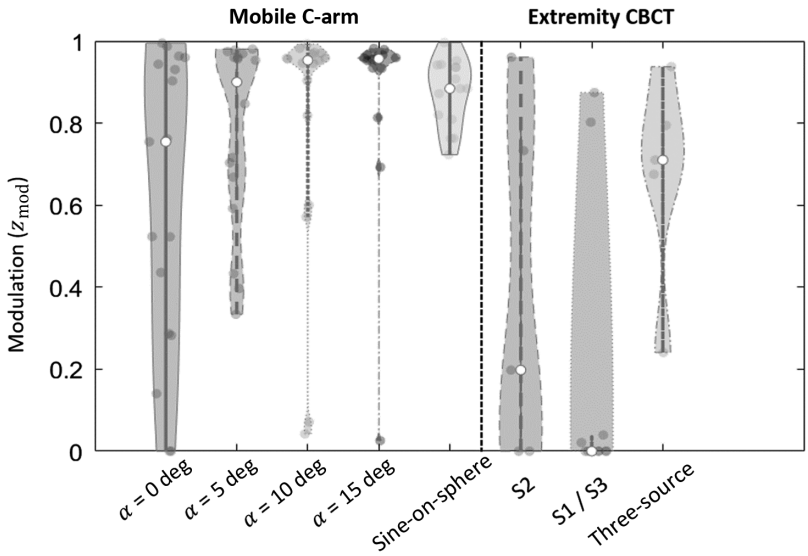

Fig. 6 Cone-beam artifact magnitude (z_{mod}) for various CBCT orbits. The first five orbits are from the mobile C-arm [i.e., left to right: circular orbit with 0 deg (untilted); 5 deg, 10 deg, and 15 deg tilt, and SoS non-circular orbit]. The last three orbits are from the extremity system (i.e., left to right: single-source orbit from S2, the single-source orbit from S1 or S3, and the three-source orbit). Each violin plot shows the underlying sample points, a Gaussian envelope, the median of the distribution (white circle), and the IQR (black vertical range bar).

to the gantry tilt. The same could be accomplished by tilting the phantom. Cone-beam artifacts (i.e., incompleteness) in general still exist throughout the volume as determined by sampling incompleteness from a single circular orbit.

Also shown in Fig. 6 is the extent to which the SoS orbit satisfies Tuy's condition for all locations within the FOV and can thus fully sample all the disk pairs, eliminating the long tail of the violin plot. The remaining spread in z_{mod} in the SoS orbit is likely due to imperfect geometric calibration and/or a lack of reproducibility in tilted scan orbits between the calibration and actual scan.

Finally, Fig. 6 shows results for various orbits possible with the extremity scanner. The "S2" configuration amounts to a single-source, circular orbit and replicates the expected result from ($\alpha = 0$ deg). The "S1/S3" orbit bi-modalizes the distribution in z_{mod}, with some disk pairs showing high modulation (at the upper or lower extrema of the FOV, close to the S1 or S3 source planes) and others throughout the middle region of the FOV exhibiting low z_{mod} associated with poor sampling completeness at high cone angles (long distance from the source planes). The three-source configuration, on the other hand, reduces cone-beam artifacts overall throughout the FOV, resulting in a narrower z_{mod} distribution compared to the single-source configurations but "washes out" the effects such that the full benefit of any single source plane is not fully realized (i.e., still exhibits undersampling from other, more distant source planes).

3.2.2 *Relating analytical models and physical measurements*

The correlation of analytical FOMs for sampling incompleteness (tan ψ_{min}) and empirical measures of cone-beam artifact magnitude (z_{mod}) is further illustrated in Fig. 7, which shows the value of tan ψ_{min} and z_{mod} along with coronal images of the corresponding disk pair at various z locations and CBCT orbits. Overall, the results are consistent with the simulations summarized in Fig. 5. For all systems and scan orbit configurations, clear correlation is observed between tan ψ_{min} and z_{mod}, suggesting z_{mod} as a reasonable surrogate for measurement of sampling/completeness effects. For the circular orbit with no tilt [Fig. 7(a)], the values of tan ψ_{min} and z_{mod} increases monotonically for both positive and negative z. Because the mobile C-arm system uses a short scan (180 deg + fan) orbit, there is a strong difference between z_{mod} distribution in z with 10 deg and -10 deg tilt angles [Figs. 7(b)–7(c)], with the former showing stronger cone-beam

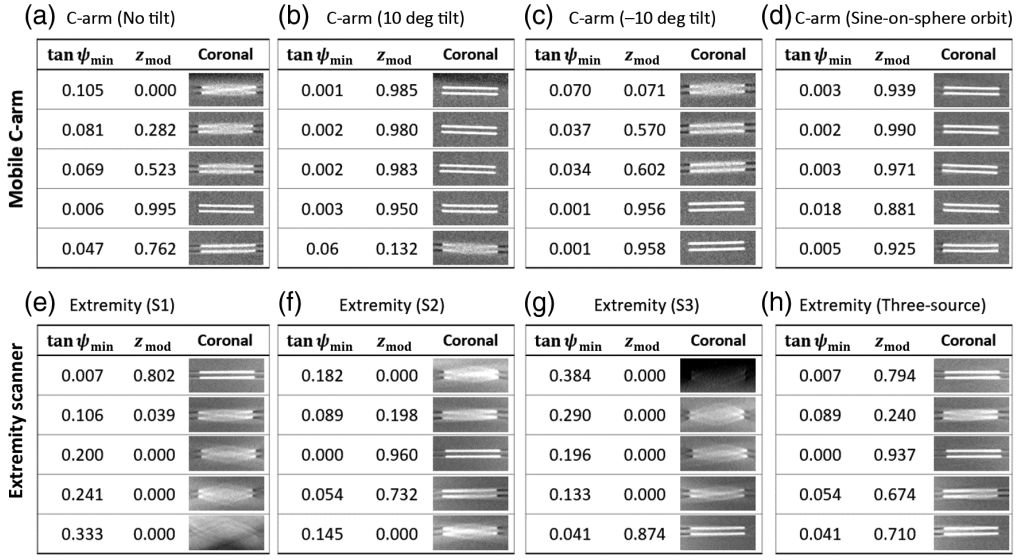

Fig. 7 Relationship of sampling incompleteness FOM [tan $\psi_{\min}$], disk-pair signal modulation (z_{mod}), and the visual appearance of cone-beam artifacts in coronal views for various CBCT orbits. For each orbit, results for various disk pairs are ordered based on ascending z location. Four orbits from the mobile C-arm system are shown: (a) untilted orbit, (b) +10 deg tilted orbit, (c) −10 deg tilted orbit, and (d) SoS orbit. Four orbits for the extremity system are also shown: (e) single-source S1 orbit (top), (f) single-source S2 orbit (middle), (g) single-source S3 orbit (bottom), and (h) combined three-source orbit.

artifacts at negative z and the latter showing stronger artifact at positive z. The SoS orbit achieves a reduction in cone-beam artifact for all disk pairs as shown in Fig. 7(d), demonstrating its superior sampling completeness.

In the extremity system, the distribution of z_{mod} with z depends on the location with respect to the activated source plane(s). In the single-source configuration (S1, S2, or S3), the location with the highest z_{mod} (least cone-beam artifact) corresponds to the activated x-ray source location. For example, in Fig. 7(e), the activated x-ray source S1 is at positive z and therefore yields improved z_{mod} in the superior portion of the FOV. In the three-source configuration, an overall increase of z_{mod} can be observed for all disk pairs; however, z_{mod} is still highest at the disk pair locations that are closest to one of the three x-ray source planes, illustrating the non-monotonic variation in sampling completeness throughout the volume and an overall averaging or "washing out" of cone-beam effects throughout the FOV.

The correlation of analytical (tan $\psi_{\min}$) and empirical z_{mod} is quantified in Fig. 8 for all orbits and disk pair locations. Overall, a monotonic correspondence between tan $\psi_{\min}$ and artifact magnitude is observed. However, Fig. 8 reveals some distinct characteristics as well. The untilted

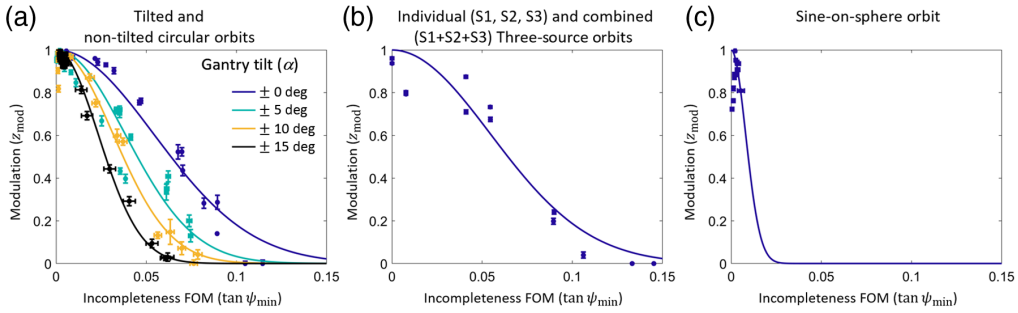

Fig. 8 Correlation of empirical z_{mod} and analytical tan $\psi_{\min}$ for various CBCT orbits. A Gaussian fit (solid line) is shown as a guide to the eye (not intended as an analytical model of relationship). (a) tilted and untilted circular orbits on the mobile C-arm. (b) Single-source S1, S2, and S3 orbits and combined three-source orbit on the extremity system. (c) SoS orbit with the mobile C-arm.

orbit [Fig. 8(a); $\alpha = 0$ deg (purple)] shows a relatively gradual reduction in z_{mod} (increased cone-beam artifact) with increasing tan ψ_{min}, with z_{mod} reduced to 0.50 at tan $\psi_{\text{min}} = 0.06$ (corresponding to an angle of ~3.5 deg). A similar relationship is observed for the tilted orbits ($\alpha = \pm 5$ deg, ± 10 deg, and ± 15 deg); however, the trend is steeper for increased tilt angle. Note also that a given value of tan ψ_{min} could relate to a range of values in z_{mod} (and vice versa), suggesting that neither FOM is a unique, unambiguous descriptor of sampling completeness or artifact magnitude. Figure 8(b) demonstrates similar correlation for various orbits on the extremity scanner (i.e., single-source S1, S2, and S3 orbits as well as the combined three-source orbit). Finally, Fig. 8(c) shows the SoS orbit to resoundingly improve cone-beam sampling completeness (uniformly low values of tan ψ_{min} and high values of z_{mod}) for all disk pairs.

3.2.3 *Implications for CBCT system design*

The trends demonstrated above provide experimental support for the notion that tan ψ_{min} conveys a meaningful, practical FOM for cone-beam sampling completeness for a range of source–detector orbits and various locations within the FOV. As tan ψ_{min} is location-dependent, one can calculate tan ψ_{min} for every location within the FOV as one aspect of CBCT system design. Figure 9 shows calculation of tan ψ_{min} as a function of (x, z) position throughout the coronal plane for various CBCT orbits. For the usual case of a single-source, untilted circular orbit [Fig. 9(a)], tan ψ_{min} (and therefore the severity of cone-beam artifacts) is minimized near the center of the FOV and increases with longitudinal position outside a fairly narrow range of ± 40 mm in [consistent with experimental measurement in Fig. 7(a)], as expected.

As shown in Figs. 9(b)–9(d), C-arm tilt extends the range over which cone-beam sampling completeness is improved (with respect to the disk pairs), and a greater portion of the coronal plane is more completely sampled. Of course, as mentioned above, that is not to say that simply tilting the orbit improves sampling completeness or removes cone-beam artifacts in general; rather, the results simply pertain to the disk pairs oriented perpendicular to the (untilted) z-axis. The same could be accomplished by tilting the disks. The underlying cone-beam sampling incompleteness is present no matter how the (circular) orbit is tilted. The artifact behavior simply "tilts" with the orbit. That said, the particular orientation considered here (disk pairs perpendicular to the untilted z-axis) is analogous to many clinical contexts, such as imaging

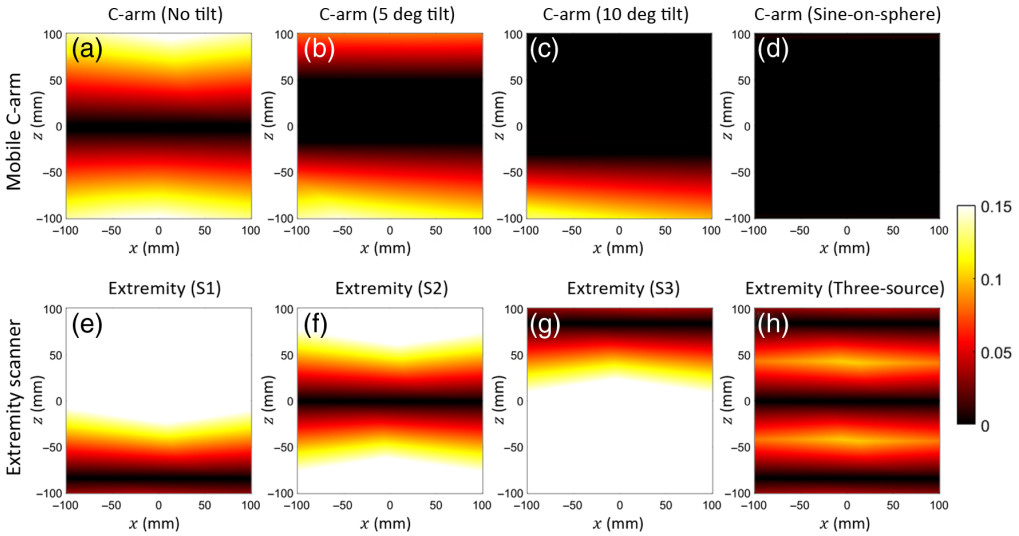

Fig. 9 Spatial dependence of tan ψ_{min} computed throughout the coronal plane for various scan orbits, illustrating how variations in orbit are related to improvement in cone-beam sampling completeness across the FOV for objects with a particular orientation. Four orbits from the mobile C-arm system: (a) untilted orbit, (b) 5 deg tilted orbit, (c) 10 deg tilted orbit, and (d) SoS orbit. Four orbits from the extremity system: (e) single-source S1 orbit, (f) single-source S2 orbit, (g) single-source S3 orbit, and (h) three-source orbit.

of vertebral endplates, the tibial plateau, or certain aspects of the skull base (e.g., cribriform plate).

The three-source orbits for the extremity scanner illustrate interesting variations on the theme: the single-source orbits (S1, S2, and S3) as shown in Figs. 9(e)–9(g), respectively, show that cone-beam artifacts are minimized in the respective source planes, but steeply increase with longitudinal position outside the source plane. The three-source orbit [Fig. 9(h)], however, imparts a non-monotonic variation in artifact magnitude throughout the volume—minimized near the source planes and increasing in between. The overall sampling completeness of the three-source orbit [Fig. 9(h)], h) is also much better ("darker" FOM map) compared to any one of the single-source orbits [Figs. 9(e)–9(g)], demonstrating the advantage of the three-source orbit.

Finally, Fig. 9(d) illustrates the effect of SoS orbit, which shows clear benefit of reduced cone-beam artifacts throughout the FOV. While only the SoS orbit was considered among many possible noncircular orbits, one can also calculate and analyze the FOM map for other emerging orbits—e.g., task-driven SNR optimization[17] or metal artifacts avoidance orbits[20,21]—which also affect the completeness of cone-beam sampling.

4 Discussion and Conclusions

The analytical basis of incompleteness in cone-beam sampling was revisited in terms of the analytical FOM $\tan \psi_{\min}$ based on established data sufficiency conditions, describing the minimum angle between a point in the 3D image reconstruction and the x-ray source for a particular source–detector orbit. This FOM is local and depends on the geometry of the system with respect to the location where the FOM was measured (i.e., is independent of the object itself). The value of $\tan \psi_{\min}$ indicates the minimal level of incompleteness that exists at the measurement location. Suitable to a broad range of arbitrary circular and non-circular orbits, this FOM was found to correlate well with the volume of the unsampled Fourier space null cone in the special case of a circular orbit (Fig. 5).

To bridge the gap between analytical FOMs and empirical measures of incompleteness in cone-beam sampling, we investigated an image quality test phantom that incorporated multiple disk pairs at various locations throughout the FOV and a corresponding empirical FOM (e.g., z_{mod}). Simulation studies showed that the z_{mod} metric is a valid surrogate for fundamental, underlying sampling/completeness effects, not an ad hoc hand-crafted metric. Moreover, it was found to be sensitive (i.e., exhibited a large dynamic range) over a range of system geometries typical of clinical CBCT.

Phantom experiments with each source–detector orbit revealed a consistent, continuous relationship between artifact magnitude and the minimum ray angle $\psi_{\min}$ at a given location in the object. While neither $\tan \psi_{\min}$ nor z_{mod} are unique descriptors of cone-beam artifact magnitude (and the latter is an empirical measure that depends on the size of the disk pairs implemented within the phantom), the work demonstrates a bridge between analytical and empirical measures of CBCT image quality. Both $\tan \psi_{\min}$ and z_{mod} can be easily computed (or for the latter, measured) for various scan orbits to provide insights on the completeness of cone-beam sampling, including not only the scenarios of untilted, circular, tilted, three-source circular, and noncircular orbits demonstrated in this work but also for novel system geometries for emerging CBCT systems and scan orbits.[14–21]

While $\tan \psi_{\min}$ was studied as the analytical FOM in this manuscript, we do not claim that $\tan \psi_{\min}$ has a stronger correlation to the empirical FOM (z_{mod}) than any other analytical FOMs previously reported in literature. For example, when only (titled) circular orbits were used, the volume of the unsampled Fourier space null cone also correlates very well with z_{mod} as demonstrated in the simulation study. However, on the one hand, $\tan \psi_{\min}$ has various advantages as mentioned in the Introduction [e.g., flexibility (compatible with non-circular orbits) and computational efficiency]. On the other hand, $\tan \psi_{\min}$ has a stronger theoretical link with the concept of resolving the gap between two parallel disks, which is exactly the definition of z direction modulation with the Corgi phantom (z_{mod}). As verified in the phantom study, there is indeed a strong link between these two analytical and empirical FOMs. Future work could include

detailed comparison between different analytical FOMs (e.g., Refs. 20, 31–35) in terms of their correlation with z_{mod} and/or other empirical task-based sampling completeness metrics.

While the experiments in this work were limited to measurement of sampling incompleteness in a certain direction (i.e., parallel to the z axis), the test phantom and the FOMs are also applicable to other directions, requiring simply that the test phantom be tilted accordingly.

The FOMs and image quality test phantom used in this article present a practical, flexible framework within which incompleteness in cone-beam sampling can be quantitatively probed, extending Tuy's condition to practical considerations of image quality and system design. The utility of the physical phantom for measurement of cone-beam sampling incompleteness is clear, demonstrating consistency with the analytical basis, and providing both visual validation and quantitative assessment of artifact magnitude in a broad variety of CBCT systems and reconstruction methods. The test phantom is suitable to physics testing in routine quality assurance and, combined with an understanding of underlying analytical considerations of cone-beam sampling incompleteness, will hopefully advance the broad understanding of factors governing image quality in CBCT.

Disclosures

No conflicts of interest, financial or otherwise, are declared by the authors.

Acknowledgments

The work was supported by the National Institutes of Health (Grant No. U01 NS-107133) and employed cone-beam computed tomography imaging systems made available through academic-industry partnership with Siemens Healthineers (Forcheim, Germany) and Carestream Health (Rochester New York, United States). The phantom was produced by The Phantom Lab (Greenwich, NY) with whom authors J. M. B. and J. H. S. hold a licensing agreement.

References

1. R. Baba, K. Ueda, and M. Okabe, "Using a flat-panel detector in high resolution cone beam CT for dental imaging," *Dentomaxillofac. Radiol.* **33**(5), 285–290 (2004).
2. J. M. Boone et al., "Dedicated breast CT: radiation dose and image quality evaluation," *Radiology* **221**(3), 657–667 (2001).
3. J. Xu et al., "Technical assessment of a cone-beam CT scanner for otolaryngology imaging: image quality, dose, and technique protocols," *Med. Phys.* **39**(8), 4932–4942 (2012).
4. P. Wu et al., "Cone-beam CT for imaging of the head/brain: development and assessment of scanner prototype and reconstruction algorithms," *Med. Phys.* **47**(6), 2392–2407 (2020).
5. W. Zbijewski et al., "A dedicated cone-beam CT system for musculoskeletal extremities imaging: design, optimization, and initial performance characterization: dedicated cone-beam CT for musculoskeletal extremities," *Med. Phys.* **38**(8), 4700–4713 (2011).
6. J. H. Siewerdsen et al., "Volume CT with a flat-panel detector on a mobile, isocentric C-arm: pre-clinical investigation in guidance of minimally invasive surgery," *Med. Phys.* **32**(1), 241–254 (2005).
7. P. Wu et al., "Reconstruction-of-difference (RoD) imaging for cone-beam CT neuro-angiography," *Phys. Med. Biol.* **63**(11), 115004 (2018).
8. R. Fahrig et al., "Flat-panel conebeam CT in the clinic: history and current state," *J. Med. Imaging* **8**(5), 052115 (2021).
9. M. Defrise and R. Clack, "A cone-beam reconstruction algorithm using shift-variant filtering and cone-beam backprojection," *IEEE Trans. Med. Imaging* **13**(1), 186–195 (1994).
10. S. Bartolac et al., "A local shift-variant Fourier model and experimental validation of circular cone-beam computed tomography artifacts: Fourier description and validation of CB artifacts," *Med. Phys.* **36**(2), 500–512 (2009).
11. R. Clackdoyle and F. Noo, "Quantification of tomographic incompleteness in cone-beam reconstruction," *IEEE Trans. Radiat. Plasma Med. Sci.* **4**(1), 63–80 (2020).
12. X. Tang et al., "On the data acquisition, image reconstruction, cone beam artifacts, and their suppression in axial MDCT and CBCT – a review," *Med. Phys.* **45**(9), e761–e782 (2018).
13. G. L. Zeng and G. T. Gullberg, "A study of reconstruction artifacts in cone beam tomography using filtered backprojection and iterative EM algorithms," *IEEE Trans. Nucl. Sci.* **37**(2), 759–767 (1990).
14. G. J. Gang et al., "Image quality and dose for a multisource cone-beam CT extremity scanner," *Med. Phys.* **45**(1), 144–155 (2018).

15. Z. Guo et al., "C-arm CT imaging with the extended line-ellipse-line trajectory: first implementation on a state-of-the-art robotic angiography system," *Phys. Med. Biol.* **65**(18), 185016 (2020).
16. P. Wu et al., "C-arm non-circular orbits: geometric calibration, image quality, and avoidance of metal artifacts," arXiv preprint arXiv:2010.00175 (2020).
17. J. W. Stayman et al., "Task-driven source–detector trajectories in cone-beam computed tomography: I. Theory and methods," *J. Med. Imaging* **6**(2), 025002 (2019).
18. J. A. Carrino et al., "Dedicated cone-beam CT system for extremity imaging," *Radiology* **270**(3), 816–824 (2014).
19. C. Zhao et al., "Cone-beam imaging with tilted rotation axis: method and performance evaluation," *Med. Phys.* **47**(8), 3305–3320 (2020).
20. G. J. Gang, J. H. Siewerdsen, and J. W. Stayman, "Non-circular CT orbit design for elimination of metal artifacts," *Proc. SPIE* **11312**, 1131227 (2020).
21. P. Wu et al., "C-arm orbits for metal artifact avoidance (MAA) in cone-beam CT," *Phys. Med. Biol.* **65**(16), 165012 (2020).
22. E. Samei et al., "Redefining and reinvigorating the role of physics in clinical medicine: a report from the AAPM Medical Physics 3.0 Ad Hoc Committee," *Med. Phys.* **45**(9), e783–e789 (2018).
23. J. H. Siewerdsen et al., "Cone-beam CT dose and imaging performance evaluation with a modular, multi-purpose phantom," *Med. Phys.* **47**(2), 467–479 (2020).
24. A. M. Hernandez et al., "Location and direction dependence in the 3D MTF for a high-resolution CT system," *Med. Phys.* **48**(6), 2760–2771 (2021).
25. P. Wu et al., "Theory, method, and test tools for determination of 3D MTF characteristics in cone-beam CT," *Med. Phys.* **48**(6), 2772–2789 (2021).
26. H. K. Tuy, "An inversion formula for cone-beam reconstruction," *SIAM J. Appl. Math.* **43**(3), 546–552 (1983).
27. H. H. Barrett and H. Gifford, "Cone-beam tomography with discrete data sets," *Phys. Med. Biol.* **39**(3), 451 (1994).
28. R. H. Johnson et al., "Feldkamp and circle-and-line cone-beam reconstruction for 3D micro-CT of vascular networks," *Phys. Med. Biol.* **43**(4), 929 (1998).
29. H. Kudo and T. Saito, "Derivation and implementation of a cone-beam reconstruction algorithm for nonplanar orbits," *IEEE Trans. Med. Imaging* **13**(1), 196–211 (1994).
30. D. V. Finch, "Cone beam reconstruction with sources on a curve," *SIAM J. Appl. Math.* **45**(4), 665–673 (1985).
31. S. D. Metzler, J. E. Bowsher, and R. J. Jaszczak, "Geometrical similarities of the Orlov and Tuy sampling criteria and a numerical algorithm for assessing sampling completeness," *IEEE Trans. Nucl. Sci.* **50**(5), 1550–1555 (2003).
32. B. Liu et al., "Completeness map evaluation demonstrated with candidate next-generation cardiac CT architectures," *Med. Phys.* **39**(5), 2405–2416 (2012).
33. F. Stopp et al., "Quality evaluation of image recording strategies for limited angle tomography," *Tsinghua Sci. Technol.* **15**(1), 25–29 (2010).
34. T. Sun et al., "Estimation of local data-insufficiency in motion-corrected helical CT," *IEEE Trans. Radiat. Plasma Med. Sci.* **1**(4), 346–357 (2017).
35. R. Clackdoyle and F. Noo, "Cone-beam tomography from 12 pinhole vertices," in *IEEE Nucl. Sci. Symp. Conf. Rec. (Cat. No. 01CH37310)*, IEEE, Vol. **4**, pp. 1874–1876 (2001).
36. A. Tersol et al., "Sampling effects for emerging cone-beam CT systems and scan trajectories: from Tuy's condition to system design and routine image quality tests," *Proc. SPIE* **12031**, 120313D (2022).
37. F. Natterer, "Computerized tomography," in *The Mathematics of Computerized Tomography*, R. E. O'Malley, Jr., Ed., pp. 1–8, Springer (1986).
38. J. A. Fessler, "Penalized weighted least-squares image reconstruction for positron emission tomography," *IEEE Trans. Med. Imaging* **13**(2), 290–300 (1994).
39. H. Erdogan and J. A. Fessler, "Ordered subsets algorithms for transmission tomography," *Phys. Med. Biol.* **44**(11), 2835–2851 (1999).
40. R. L. Siddon, "Fast calculation of the exact radiological path for a three-dimensional CT array," *Med. Phys.* **12**(2), 252–255 (1985).
41. T. M. Peters, "Algorithms for fast back- and re-projection in computed tomography," *IEEE Trans. Nucl. Sci.* **28**(4), 3641–3647 (1981).
42. N. M. Sheth et al., "A mobile isocentric C-arm for intraoperative cone-beam CT: technical assessment of dose and 3D imaging performance," *Med. Phys.* **47**(3), 958–974 (2020).
43. Y. Cho et al., "Accurate technique for complete geometric calibration of cone-beam computed tomography systems: accurate technique for geometric calibration of cone-beam CT systems," *Med. Phys.* **32**(4), 968–983 (2005).
44. X. Tang and R. Ning, "A cone beam filtered backprojection (CB-FBP) reconstruction algorithm for a circle-plus-two-arc orbit," *Med. Phys.* **28**(6), 1042–1055 (2001).

45. N. Gindrier, L. Desbat, and R. Clackdoyle, "CB reconstruction for the 3-sin trajectory with transverse truncation," in *16th Virtual Int. Meeting on Fully 3D Image Reconstruct. in Radiol. and Nucl. Med.* (2021).
46. J. D. Pack, F. Noo, and H. Kudo, "Investigation of saddle trajectories for cardiac CT imaging in cone-beam geometry," *Phys. Med. Biol.* **49**(11), 2317 (2004).

Pengwei Wu received his BE degree in electrical engineering from Zhejiang University in 2016 and his PhD in biomedical engineering from Johns Hopkins University in 2022. He is currently a research scientist at GE Healthcare Research. His research interests involve analytical, model-based, and deep learning algorithms for medical imaging applications, especially for x-ray and CT systems.

Aina Tersol received her MSE degree in biomedical engineering from Johns Hopkins University. She is a biomedical engineer and machine learning data scientist at SignalPET, LLC. She specializes in developing and implementing AI algorithms, specifically for medical imaging applications. Her work encompasses x-ray imaging quality analysis, AI interpretability, image classification, segmentation, and pattern recognition.

Rolf Clackdoyle's field of research is tomographic image reconstruction using analytic methods, with applications in X-ray CT, in PET, and in SPECT. He received his master's degree from Queen's University, Canada, and his PhD from Dalhousie University, Canada. He was assistant, associate, and full professor of radiology at the University of Utah, before moving in 2004 to a research director position in France. He is currently at the TIMC laboratory, Univ. Grenoble Alpes.

John M. Boone is a professor of radiology and biomedical engineering at the University of California Davis. His research interests include the development of breast imaging technology including breast computed tomography and multiple x-ray source array systems for breast tomosynthesis. He has published extensively on radiation dose in mammography and computed tomography, and led a team to develop the size specific dose estimate (SSDE) for CT, which has become a standard metric for CT dose reporting.

Jeffrey H. Siewerdse received his PhD in physics from the University of Michigan, and worked previously at William Beaumont Hospital, Ontario Cancer Institute, and Johns Hopkins University, where he was a professor and vice-chair in biomedical engineering. He is now head of the Surgical Data Science Program and a professor of imaging physics at the University of Texas MD Anderson Cancer Center. His research involves the physics of image quality and development of technologies and algorithms for cone-beam CT.